

---

# PATHOINSIGHTMIL: A DEEP LEARNING FRAMEWORK FOR UNVEILING COLON CANCER THERAPY RESISTANCE IN HISTOPATHOLOGY IMAGES

---

## ABSTRACT

Resistance to cancer therapy and subsequent relapse are often driven by a subpopulation of tumor cells that are temporarily arrested in a 'G0-arrest' state as they evade anti-cancer compounds which target actively dividing cells, facilitating minimal residual disease. We developed a comprehensive and versatile weakly-supervised learning framework, PathoInsightMIL, instantiated in this work to assist biologists study therapy resistance solely from colorectal whole-slide images, serving as a cost-effective alternative to sequencing technologies. PathoInsightMIL encompasses the preprocessing of slides, benchmarking of state-of-the-art multiple-instance learning algorithms through cross-validation, and interpretability analysis. PathoInsightMIL supports the use of foundation models, classification through multimodal fusion of clinical features, and regressing biomarker scores as a more expressive alternative to predicting discrete labels. Through a dataset of 578 colorectal tissue sourced from TCGA, we achieve a classification performance of AUROC of 0.829 and F1 score of 0.724 through an ensemble of TransMIL models obtained from 5-fold cross-validation. Subsequent heatmap visualization over the tissue showed clusters of both proliferating and G0-arrest cell populations, and input feature attribution helped elucidate how clinical features influence the decision boundary. We contribute the code for PathoInsightMIL with experiments written with the HistoMIL package at <https://github.com/awxlong/HistoMIL> to the community. It serves as a generalizable framework to streamline further research in computational histopathology through multiple-instance learning.

## 1 Introduction

Colorectal cancer (CRC) ranks as the third most commonly diagnosed cancer, and the second leading cause of cancer associated mortality worldwide, with over 1.9 million new cases and more than 930000 deaths estimated in 2020 [Alboaneen et al., 2023, Sallinger et al., 2023]. The World Health Organization projects that by 2040, the burden of CRC will increase to 3.2 million new cases per year and 1.6 million deaths per year, reflecting increases of 63% and 73%, respectively. CRC predominantly affects older individuals, with most cases occurring in people aged 50 and above. One of the main drivers of poor survival in patients is post-surgery recurrence. It has been reported that 20 – 50% of patients with CRC will relapse after curative resection [Xiao et al., 2024], with rates varying depending on several factors such as metastatic pattern, tumor anatomical sublocation, and surveyed population [Qaderi et al., 2021, Safari et al., 2023]. Altogether, this underscores an urgent need for improved diagnostics through an understanding of cancer recurrence.

'**G0-arrest**' cells (also referred to as 'dormant') have been garnering the attention of the research community for their critical role in relapse. When cells exit their normal replicative cycle into a state of G0-arrest, although they might be metabolically active, they cease to grow and have reduced rates of protein synthesis. These cells are 'quiescent' if they can revert to the cell cycle from G0-arrest, otherwise 'senescent'[Cooper, 2000]. Crucial to entry to G0-arrest is the inhibition of cyclin-dependent kinases [Pack et al., 2019]. This dormancy can be caused by a variety of factors, whether it's induced through environmental stress as shown by simulations from in-vitro models [Mitra et al., 2018], replicative stress, oncogene activation, or could be a natural stage of a cell's developmental process [Oki et al., 2014]. Dormancy grants cells resistance to anti-cancer compounds because they are unlikely to induce non-replicating functional DNA, making them insensitive to chemotherapy-related DNA damage agents which are designed to target proliferating cells [Chen et al., 2022a]. Furthermore, dormant cells have been shown to evade immune

surveillance as they can interpret homeostatic signals from the microenvironment [Park and Nam, 2020]. They also exhibit remarkable adaptability to new environmental niches during metastatic seeding. Altogether, they facilitate minimal residual disease, becoming a major factor associated with cancer relapse once they reawaken from G0-arrest and start proliferating [Wiecek et al., 2023]. Moreover, it has been estimated that more than 80% of internal cancer cells within a tumor are in a quiescent state, leading to ineffective elimination of solid tumors. Notably, studies have also shown that anticancer therapy can increase the proportion of dormant cancer cells, further contributing to chemoresistance after treatment cycles [Lindell et al., 2023]. Such prevalence underscores the necessity for advanced methodologies to gauge these dormant populations in order to understand their role in therapeutic resistance.

Consequently, [Wiecek et al., 2023] developed through a pan cancer-tissue analysis a transcriptional signature for identifying G0-arrest cells from bulk and single-cell RNA-sequencing data. Monitoring this state in a tumor through sequencing technologies can help study therapeutic resistance. However, on one hand, bulk-RNA sequencing of cancer tissue is not spatially resolved, and thus obscures the contributions of individual cell types and their interactions within the tumor-microenvironment (TME). On the other-hand, single-cell and spatial transcriptomics (ST) techniques are expensive and are limited in cell coverage compared to whole-slide images (WSIs) [Levy-Jurgenson et al., 2020]. Furthermore, sequencing technologies, especially spatially-resolved ones, may face several hurdles for routine usage to their novelty, associated costs, and the demand for relevant experienced personnel. As such, in this study, we propose PathoInsightMIL, a comprehensive deep learning-based framework to act as a computational alternative that can predict both the state of G0-arrest solely from hematoxylin and eosin (H&E) tissue and provide a spatially resolved explanation to such prediction, proving a more accessible alternative than sequencing the tissue.

## 2 Literature review

**Deep learning for molecular-level predictions.** In oncology, deep learning (DL) models have demonstrated exceptional capabilities in feature extraction from complex, high-dimensional data like WSIs, which has enabled precise and timely diagnosis, treatment planning, biomarker identification, localization, (pan-)cancer subtype classification, and prognosis prediction [Song et al., 2023, Tran et al., 2021, Couture, 2022, Lee, 2023]. Owed to the unique challenges of WSIs, namely their gigapixel size and annotation burden, the prevalent paradigm is to analyze them through *multiple-instance learning* (MIL) (see definition in Appendix A). The general pipeline consists of WSI preprocessing: tissue segmentation and patching [Lu et al., 2021]. This is followed by feature extraction which can be done through a model pre-trained through (contrastive) self-supervised learning (SSL) [Schirris et al., 2022]. For computational efficiency, one can instead extract features leveraging off-the-shelf pretrained models like ResNet [Lu et al., 2021, Hezi et al., 2024], CTransPath [Wagner et al., 2023] or REMEDIS [Azizi et al., 2023]. This is followed by training within a cross-validation framework [Lu et al., 2021, Yacob et al., 2023, Zheng et al., 2022, El Nahhas et al., 2024] where WSI features are aggregated through max or average pooling before making a histological or molecular-level prediction like detecting the presence of cancer [Alboaneen et al., 2023] or classify tumor-immune cells [Parreno-Centeno et al., 2022]. Alternatively, attention-based MIL [Ilse et al., 2018] enables learning the relative importance of patches before pooling for a bag-level decision, enhancing predictive performance with improved interpretability. On tasks like microsatellite instability (MSI) classification on surgical resection specimens, attention-based MIL reaches clinical-grade performance on endoscopic biopsy [Wagner et al., 2023].

In the context of studying cancer relapse, most work has focused on predicting proliferation biomarkers. [Martino et al., 2024] proposed using conditional adversarial network to identify Ki-67, a protein associated with the G1, S, G2, and M phases of the cell cycle, from H&E images of oral squamous cell carcinoma. A large scale, systematic pan-cancer study by [Arslan et al., 2024] benchmarked 13443 DL models to predict 4481 multiomic biomarkers across 32 cancer types, and they reported high predictive capability of cell proliferation biomarkers, particularly for breast, stomach, colon, and lung cancers, with areas under the receiving operating characteristics (AUROC) reaching up to 0.854. However, it is only in recent years that the understanding of cancer relapse has increasingly focused on the role of G0-arrest and dormancy-associated therapeutic resistance. This shift highlights the importance of dormant cancer cells, which can evade treatment and contribute to tumor recurrence. Moreover, to the best of our knowledge, there has yet to be prior work attempting to predict a biomarker for cell dormancy from colorectal WSIs, representing a significant gap in the literature that we aim to fill with DL to assist the research community in studying therapeutic resistance.

**Regression vs. classification.** A notable innovation concerns resorting to regression instead of solely focusing on classification. [El Nahhas et al., 2024] propose a model which predicts the Homologous Recombination Deficiency (HRD) biomarker scores rather than categorical labels of cells in H&E images. They argued that biomarkers of key cancer processes are continuous measurements, and binarizing them result in information loss that may hamper a classifier's performance. Through their experiments, they found that regression significantly enhanced the accuracy

of spatially resolved, HRD prediction, and offered a higher prognostic value than classification-based labels. For our purposes, because both HRD and G0-arrest stage can be expressed as continuous scores, we explore predicting G0-arrest scores in addition to classification.

**Spatial inductive bias.** Most MIL algorithms assume permutation invariance of image patches [Ilse et al., 2018], neglecting their spatial dependency. Recent work has sought to address this limitation via imposing a topological constraint over the input space by representing the WSI as a graph, where patches are nodes and edges only connect neighboring patches. This enables attention computation to focus solely on adjacent tiles, capturing features on localized areas of the slide [Zheng et al., 2022, Fourkioti et al., 2024, Shi et al., 2024]. Most work, however, only discuss the performance benefits of placing this topological prior. Through our framework, we also highlight implications of biological significance through interpretability analysis comparing MIL algorithms with and without the spatial constraint.

**Foundation models for histopathology.** There is a growing interest foundation models stemming from their ability to leverage vast and diverse datasets for self-supervised learning, resulting in context-dependent and semantically rich feature representations [Vorontsov et al., 2023]. [Chen et al., 2024] propose UNI, a foundation model based on the Vision Transformer (ViT) pretrained through SSL using more than 100 million images from over 100000 diagnostic H&E -stained WSIs across 20 major tissue types. [Xu et al., 2024] propose Prov-GigaPath, which employs a scalable variant of the ViT (called LongNet), is pretrained on 1.3 billion  $256 \times 256$  pathology image patches in 171189 WSIs spanning 31 major tissue types. Both models achieved state-of-the-art (SoTA) classification performance when fine-tuned to cancer subtyping tasks. However, finetuning either foundation model to our novel task of G0-arrest classification would be prohibitively expensive and require a multi-GPU setup. As such, within PathoInsightMIL, they are integrated as powerful, frozen feature extractors, which help train MIL algorithms with high prospects of generalization [Chen et al., 2024].

**Multimodal fusion.** The rationale behind multimodal fusion is to train a model able to capture cross-modality interactions with the hope of improving the model’s predictive expressivity and accuracy [Feng et al., 2024]. [Chen et al., 2022b] propose a pan-cancer model integrating WSI with genomic data through late fusion of embeddings to estimate patient survival, elucidating advantages such as mostly outperforming unimodal approaches and improved model explainability thanks to the joint analysis of image and genomic features. Their method is used by [Volinsky-Fremond et al., 2024] to combine tumor stage with endometrial H&E WSI embeddings for predicting recurrence risk. In our work, we explore the fusion of a mix of continuous and categorical clinical variables with the WSI to predict dormancy. Furthermore, interpretability analysis is carried out through input feature attribution [Sundararajan et al., 2017] to explore the influence of each clinical feature on the G0-arrest decision boundary.

### 3 Methodology

PathoInsightMIL seeks to balance utility in terms of training MIL models which achieve high predictive performance, but also at an efficient computational cost coupled with transparent biological analysis. Thus, our framework, which builds upon [Lu et al., 2021], is designed as in Figure 1. It is split into 3 stages: 1) feature extraction through pre-trained models, 2) benchmarking attention-based models under 5-fold cross-validation, exploring ablations (including regression, multimodal fusion and spatial inductive bias) and ensembling at inference time, and 3) post-hoc evaluation including examining test results and interpretability analysis.

#### 3.1 Feature extraction per WSI and patient

We obtain 578 colorectal adenocarcinoma, H&E stained WSIs from The Cancer Genome Atlas (TCGA), each matched with bulk-RNA sequencing data. By employing the genomic signature of [Wiecek et al., 2023], each colon WSI is given a label  $s$  (see Appendix Equation 2). If it’s continuous,  $s$  is a score indicating level of quiescence. This score is binarized based on a clinical threshold, whereby if it’s negative ( $\leq 0$ ),  $s = 1$  indicating the presence of cells in G0-arrest in the WSI, and if positive ( $> 0$ ), it represents absence of such.

PathoInsightMIL preprocesses one WSI following the segmentation and patching protocol at [Lu et al., 2021], where we choose a patch size of  $(224 \times 224)$  with no overlap. We proceed to store a matrix representation  $\mathcal{W} \in \mathbb{R}^{N \times D}$  by stacking  $D$ -dimensional feature vectors computed per each of the  $N$  patches of a WSI for each of the following feature encoders: ResNet50 ( $D = 2048$ ), UNI ( $D = 1024$ ) and Prov-Gigapath ( $D = 1536$ ). We do this for each of our WSI, where we note that 1)  $N$  is different per slide due to morphologically different tissue per person or anatomical site, and 2) it can range between  $[10000, 120000]$ . In the interest of training some MIL algorithms with topological constraints, a cropped WSI is also represented with an undirected graph  $G = (V, E)$  where vertices  $V$  correspond to

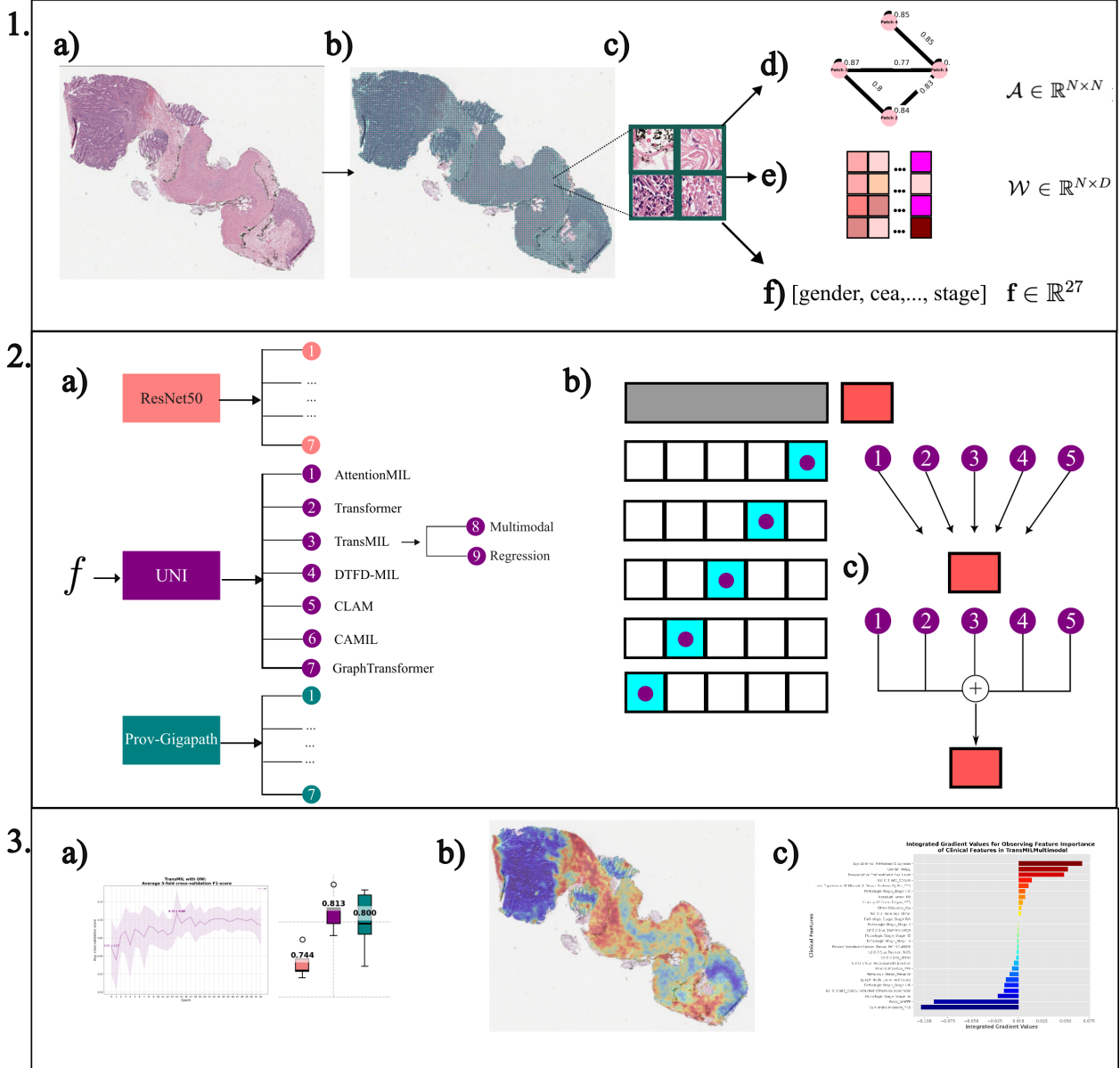


Figure 1: Depiction of the PathoInsightMIL pipeline. First, preprocessing for 1.a) each colorectal WSI consists of 1.b) tissue segmentation and 1.c) patching. We then compute 1.d) topological constraints, 1.e) patch-wise feature extraction, and 1.f) preprocessing of clinical features. Afterwards, 2.a) SoTA MIL algorithms are trained and evaluated through 2.b) cross validation. At test time, 2.c) we obtain conformal predictions and build an ensemble of models from cross-validation. Lastly, at 3.a) we report evaluation results. We perform interpretability analysis based on 3.b) heatmap visualization, and at 3.c) clinical feature attribution.

image patches, and  $(v_i, v_j) \in E$  are pairwise edges of patches that are adjacent to one another, where in WSIs each patch has at most 8 neighboring patches.  $G$  is represented via a weighted adjacency matrix  $\mathcal{A} \in \mathbb{R}^{N \times N}$  per WSI, where  $\mathcal{A}_{ij} = a_{ij}$  according to the following equation 1:

$$a_{ij} = \begin{cases} \exp(-(\mathbf{h}_i - \mathbf{h}_j)^2) & \text{iff } (v_i, v_j) \in E, (\mathbf{h}_i, \mathbf{h}_j) \in \mathcal{W} \\ 0, & \text{otherwise} \end{cases} \quad (1)$$

, where a distance similarity score is computed only if two patches are adjacent to one another, and 0 otherwise. This similarity score is the exponentiated, normalized, Euclidean distance between the feature representations of 2 patches, which injects a bio-topological prior constraint that drives MIL models to attend to patches close and similar to each other [Fourkioti et al., 2024].

Our WSIs belong to 570 unique patients as for some of them, tissue from multiple anatomical locations was collected. Since we explore multimodal fusion later in our work, we collect the following clinical features  $\mathbf{f} \in \mathbb{R}^{27}$  per patient: patient's age, lymph node count, preoperative CEA level, gender, race, other diagnoses, pathological stage, histological site, neoplasm cancer status, venous invasion, lymphatic invasion, history of colon polyps, residual tumor and loss of expression of mismatch repair (MMR). We discuss in detail the selection and preprocessing of the above features at the Appendix D, which involve technicalities such as normalization and mode imputation whilst avoiding train-test leakage, grouping of variables to address class imbalance, one-hot encoding, shadow-based feature selection, among others.

### 3.2 Benchmarking models under 5-fold CV

We perform a 90% – 10% train-test split, along with 5-fold cross validation (CV). In contrast to prior work, we employ CV not for hyperparameter tuning nor neural architectural search since that would be prohibitively expensive and cumbersome given our limited GPU cluster resources. Rather, CV is 1) used to get uncertainty estimates of a model's generalization performance through conformal predictions, and 2) obtaining independent fold models to build an ensemble for predicting over the test set [El Nahhas et al., 2024].

At each fold, for each feature encoder, we benchmark the following MIL algorithms chosen based on their novelty, reported SoTA performance and ease of adoption with HistoMIL: AttentionMIL [Ilse et al., 2018], Transformer [Wagner et al., 2023], TransMIL [Shao et al., 2021], DTFD-MIL[Zhang et al., 2022], CLAM [Lu et al., 2021], CAMIL [Fourkioti et al., 2024] and Graph Transformer [Zheng et al., 2022]. With TransMIL, we also explore multimodal fusion (TransMILMultimodal) of the clinical features above through late fusion, which consists of passing embeddings through a gated attention mechanism for automatic regularization, followed by the Kronecker product to model pairwise interactions [Chen et al., 2020]. We also explore regression (TransMILRegression), which consists of changing the output of the original TransMIL from a class probability with a range of  $[0, 1]$  to a logit with a theoretical range of  $[-\infty, +\infty]$ . This is accompanied by changing a classification loss function with a regression-based mean-squared error (MSE), along with providing G0-arrest ground truth scores instead of binarized labels<sup>1</sup>.

All the above models, except in TransMILRegression which uses the MSE, are trained by minimizing the binary cross-entropy loss with logits (BCEWithLogits). For all algorithms we train with mixed-precision, a batch size of  $1^2$ , and gradient accumulation over 4 batches to simulate a batch-size of 4, giving us the smoothness and convergence speed of mini-batch optimization. Furthermore, all models, except the Transformer, can complete their 5-fold CV in  $\leq 16$  GB of GPU memory in less than 3 days. The Transformer is the only which uses an A40 (48 GB of GPU memory), and completes the 5-fold CV regime in less than 6 hours. We reuse the hyperparameters mentioned in each MIL algorithm's paper. For specific details, please see Appendix E.

For evaluation, we report AUROC and the F1-score [Schirris et al., 2022]. For TransMILRegression, where outputs stop being probabilities, we compute instead the Pearson's correlation coefficient (PCC) [El Nahhas et al., 2024]. Because we can binarize scores at a clinical threshold of 0, we can compute its F1 and compare it across all models benchmarked. Additionally, we also measure performance metrics like validation/test loss, accuracy, precision, specificity, and recall. We also monitor training accuracy and loss to check for training stability and convergence.

### 3.3 Post-hoc analysis

Interpretability analysis is done in 2 ways. For all MIL algorithms models except TransMILMultimodal which consists of clinical features, we trace the attention scores back to the original patches they correspond to explain the model output,

---

<sup>1</sup>We only pick TransMIL with the UNI feature encoder to explore multimodal fusion and regression for 2 reasons: it achieves the second highest mean CV F1-score, preceded by the Transformer, and it's affordable to train within 16 GB of GPU memory, unlike the Transformer which requires at least 48 GB

<sup>2</sup>This is because we can't stack  $\mathcal{W}$  as  $N$  is different per slide

	<b>ResNet50</b>		<b>UNI</b>		<b>Prov-Gigapath</b>	
	AUROC	F1	AUROC	F1	AUROC	F1
<b>Transformer</b>	0.759	0.710	<b>0.859</b>	<b>0.780</b>	0.841	0.737
<b>TransMIL</b>	0.751	0.737	0.829	0.724	0.812	0.750
<b>DTFD-MIL</b>	0.754	0.689	0.831	0.720	0.828	0.741
<b>CAMIL</b>	0.772	0.719	0.779	0.667	0.816	0.746
<b>CLAM</b>	<b>0.794</b>	<b>0.759</b>	0.776	0.679	<b>0.844</b>	<b>0.750</b>
<b>AttentionMIL</b>	0.751	0.600	0.779	0.600	0.812	0.654
<b>GraphTransformer</b>	0.325	0.507	0.702	0.667	0.602	0.714

Table 1: Scores obtained from ensemble predictions on the test set. Ensemble consists of the best models per each CV fold which maximized AUROC. In bold we highlight the highest metric across algorithms (column-wise), and in italics we highlight the highest metric across feature encoders (row-wise). This is, the Transformer architecture with the UNI feature encoder achieves the highest test performance.

adopting the method by [Lu et al., 2021]. Since cells are either proliferating or in G0-arrest (i.e. mutually exclusive states), patches with high attention scores likely contain G0-arrest cells, while those with low scores correspond to normal-cycling cells.

For TransMILMultimodal, which incorporates clinical features, we employ Integrated Gradients (IG) [Sundararajan et al., 2017] to assess each feature’s influence on the model’s predictions, following the approach of [Volinsky-Fremond et al., 2024]. IG attributes a model’s prediction to its input features by integrating the gradients along a path from a baseline to the actual input. In our case, the baseline is a 27<sup>th</sup>-dimensional zero vector representing a non-informative state. Features with higher absolute IG values have a greater impact on the slide-level prediction of G0-arrest, else otherwise.

All relevant code for PathoInsightMIL is written in HistoMIL, and found at <https://github.com/awxlong/HistoMIL>, with scripts for running experiments at [https://github.com/awxlong/scripts\\_g0\\_arrest](https://github.com/awxlong/scripts_g0_arrest)

## 4 Results and Discussion

### 4.1 Ensemble modeling and foundation feature encoders help with generalization

We benchmark the MIL models and evaluate them on their predictive accuracy on G0-arrest. Our CV results are at Appendix B. In our work, our most performant algorithms can consistently achieve an AUROC greater than 0.75 and F1 greater than 0.65. The ensembles we built achieved a test performance shown in Table 1. The ensemble results for each of TransMIL’s ablations are at Table 2. In accordance to the literature, ensembling generally improved performance compared to individual models (Figures 3, 10, 11), albeit at the expense of lacking confidence intervals in their predictions.

Unlike prior work which mainly uses ensembling for performance gain, we further examined how ensemble-generated heatmaps differ from those of single models’. Ensemble heatmaps are generated by averaging the attention scores from each CV model and overlaying them over the WSI. For instance, for TransMIL, we observe how ensembling helps correct a previously wrong prediction made by the single best TransMIL (Figure 2). For a slide labeled 1, the ensemble’s heatmap identified more G0-arrest regions and attenuated previously overconfident proliferation areas.

In contrast to prior work on foundation models which focuses on training and fine-tuning them, we demonstrate a cost-efficient usage by treating them as WSI feature extractors. In our work, our test results (Figures 3, 10) showed MIL algorithms trained with foundation feature encoders often lead to better generalization performance. Such phenomenon is explained by the foundation models being subjected to an extensive pretraining regime localized to histopathology, as opposed to ResNet and its variants which are pretrained on generic images.

Subsequent interpretability analysis provides a spatially-resolved explanation consisting of heatmaps demarcating cell populations per patch leading to a slide-level prediction (Figure 4). We also show a more comprehensive view of heatmaps generated by our Ensemble TransMIL in the Appendix Figure 12, encompassing correct and incorrect predictions, along with sample patches informing the ensemble’s decisions.

### 4.2 Multimodal fusion improves interpretability with some performance sacrifice

We built an Ensemble TransMILMultimodal which achieved slightly lower test AUROC and F1 compared to the original TransMIL (Table 2). However, the incorporation of clinical features enable analyzing their IG values. We

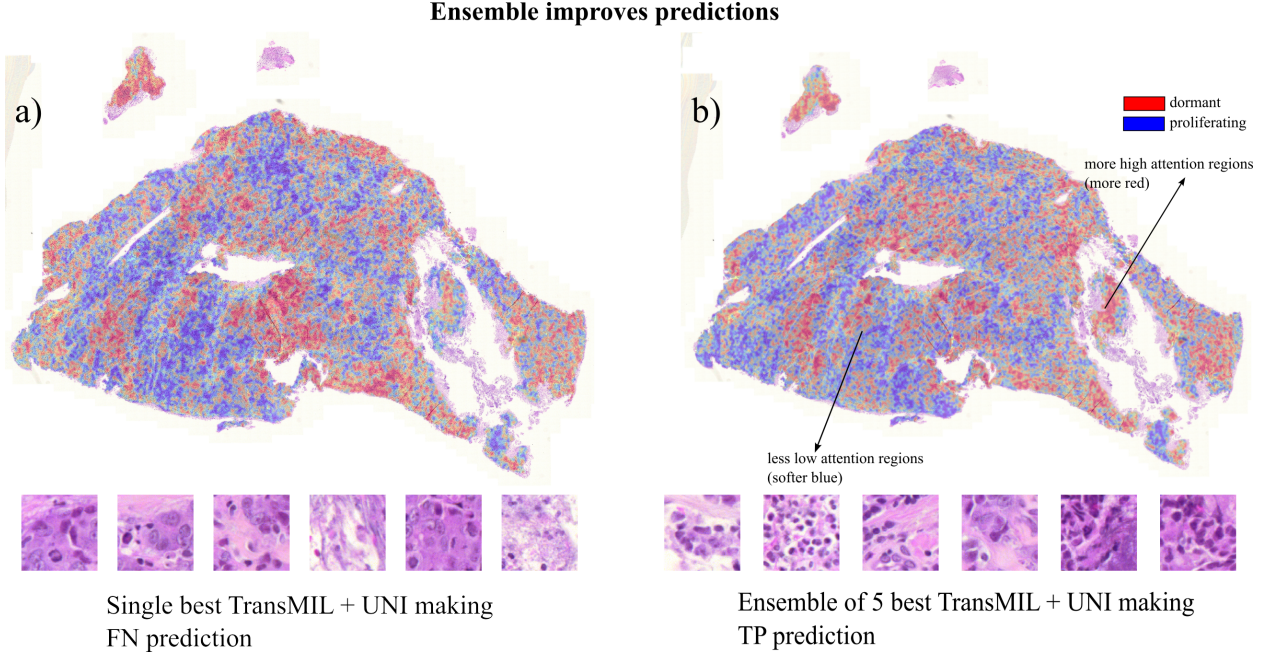


Figure 2: Depiction of how an ensemble improves predictions, and this is reflected in the heatmaps generated. At a) we show a single TransMIL trained with the UNI feature encoder making a false negative prediction on a testpoint. At b), this is corrected into a true positive prediction by an ensemble of the 5 optimal TransMIL according to each of their best validation AUROC achieved per CV fold. The ensemble is able to identify more regions with high likelihood of G0-arrest cells, while decreasing its belief of the presence of normal-cycling cells in the same regions the single TransMIL believed otherwise. The sampled patches in a) correspond to those with low attention scores, and those in b) are those with high attention scores due to the mutual exclusivity assumption.

observe that a lot of features, particularly categorical ones like ICD-O-3 site and Pathological Stages mostly lose their relevance (i.e. average IG value close to 0) for predicting G0-arrest. This is perhaps due to much heterogeneity which drives the model prioritize morphological and other clinical features instead. Regardless, we particularly observe Pathological Stage IIA (classified under Early Stage) being associated to a negative G0-arrest prediction. This is consistent with current views of pre-metastasis cancer cell behavior arguing that tumor cell dissemination can occur in the very early stages of disease, long before a tumor is even palpable [Attaran and Bissell, 2021, Lawrence et al., 2023]. On the other hand, TransMILMultimodal identified Pathological Stage IIIC (Late Stage cancer) as having on average a positive IG, driving the model to predict a high likelihood of G0-arrest populations in the CRC tissue. While late-stage cancers are typically characterized by aggressive growth and metastasis [Lawrence et al., 2023], disseminated tumor cells can become dormant at any stage and reactivate due to tumor microenvironmental changes or therapeutic stress [Truskowski et al., 2023].

Relevant clinical features learnt by TransMILMultimodal with non-zero IG values include a patient's age, gender and preoperative CEA level. High preoperative CEA level ( $> 10 \text{ ng/mL}$ ) is a well-established prognostic biomarker associated with a higher risk of recurrence and metastasis in CRC[Lai et al., 2023]. Additionally, age has prompted much research regarding CRC progression and treatment outcomes [Cho et al., 2021]; for instance, age-related biological changes in immune response ('immunosenescence') [Thoma et al., 2021] leads to older patients being associated with higher prevalence of senescent T cells, which are less effective at responding to tumors. Furthermore, research has corroborated the existence of sexual dimorphism with regards to CRC response to treatment efficacy or toxicity [Baraibar et al., 2023], or survival advantages [Geddes et al., 2022], which could be partly explained by an interplay of senescent and proliferating cells.

The literature on the understanding of CRC recurrence is nuanced and multi-faceted, and generally it's inconclusive whether it's driven mainly through tumor proliferation or reactivation of dormant tumor cells. Thus, our heatmaps and multimodal analysis offer valuable insights for clinical pathologists to navigate this complicated tumor landscape.

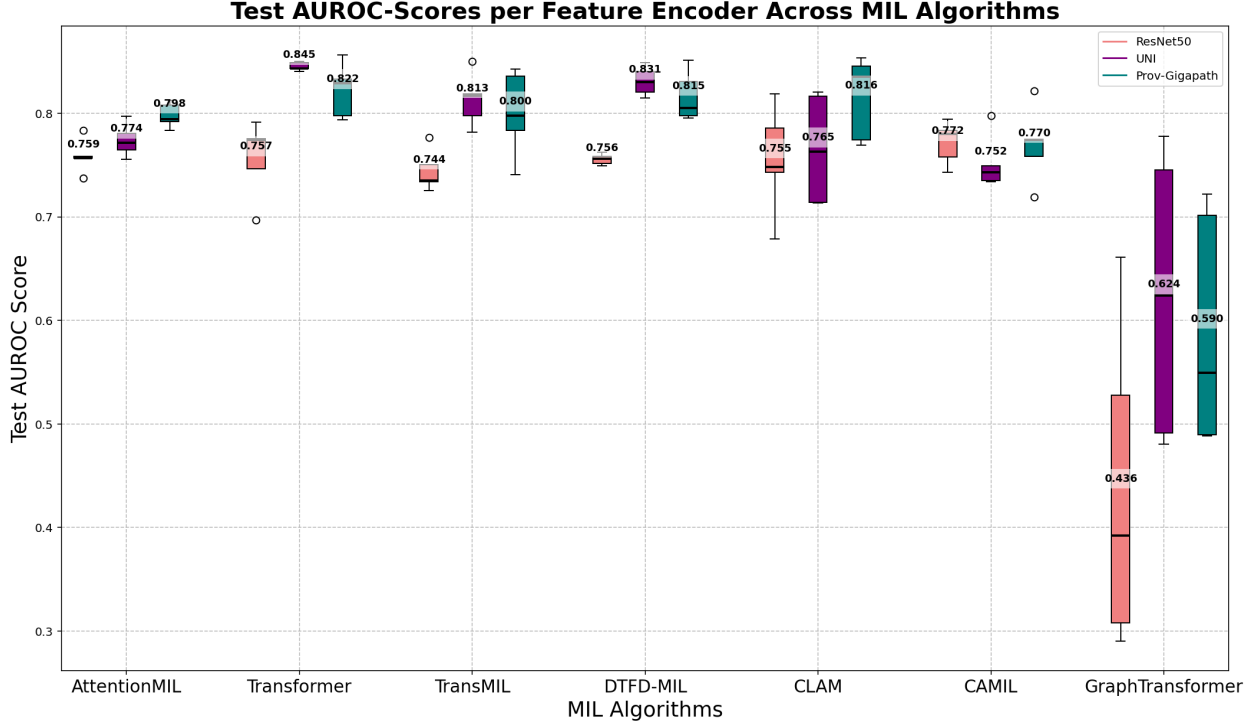


Figure 3: Average test AUROC obtained from the 5 independent optimal models per fold, per feature encoder. We notice that for all algorithms, except CAMIL, at least one of both foundation feature encoders surpasses the performance of the ResNet50 encoder, albeit with overlapping std. errors (i.e. in the figure the purple and teal bars are often higher than their lightcoral counterpart). This suggests that the choice of foundation feature encoders helps with generalization.

	AUROC	F1	PCC
<b>TransMIL</b>	0.829	0.724	N/A
<b>+ Multimodal</b>	0.805	0.679	N/A
<b>+ Regression</b>	N/A	<b>0.786</b>	0.312

Table 2: Scores obtained from ensemble predictions on the test set. Ensemble consists of the best models per each CV fold which maximized AUROC. For multimodal and regression, we only perform experiments on TransMIL using the UNI feature encoder. For regression, we note that only PCC is available to measure the correlation of the continuous predictions with the G0-arrest scores. F1 is measured via binarizing the regression scores with a clinical threshold of 0 and comparing with the binary ground truth labels. The first row is the same as in Table 1. We obtain the highest F1 through binarizing regression scores.

### 4.3 Inductive biases yield more biologically meaningful predictions

**Spatial context-awareness** Prior work on graph-based approaches to MIL mainly highlighted performance benefits. Through interpretability analysis in this work, we further demonstrate that the topological constraints of CAMIL and GraphTransformer enable visualizing more pronounced clusters of cell populations, while for alternatives they are more scattered. This aligns closer to biological expectations regarding proliferating and quiescent cells forming clusters (see a closer look at Figure 6). The drop in performance could be explained as follows: if individual patches were misidentified to contain G0-arrest cells, then adjacent patches would also be considered to erroneously contain them due to the adjacency constraints that make neighboring patches influence each other.

**Biological continuum awareness** While our Ensemble TransMILRegression results showed poor PCC with regards to ground truth scores (Table 2), interestingly, if we train the model through regression and binarize the output scores, Ensemble TransMILRegression achieved the highest test F1 (0.786) amongst all the models benchmarked. Thus, our work supports conclusions drawn by [El Nahhas et al., 2024], whereby learning to predict G0-arrest scores instead of dichotomized labels leads to higher performance by capturing a more nuanced biological spectrum.

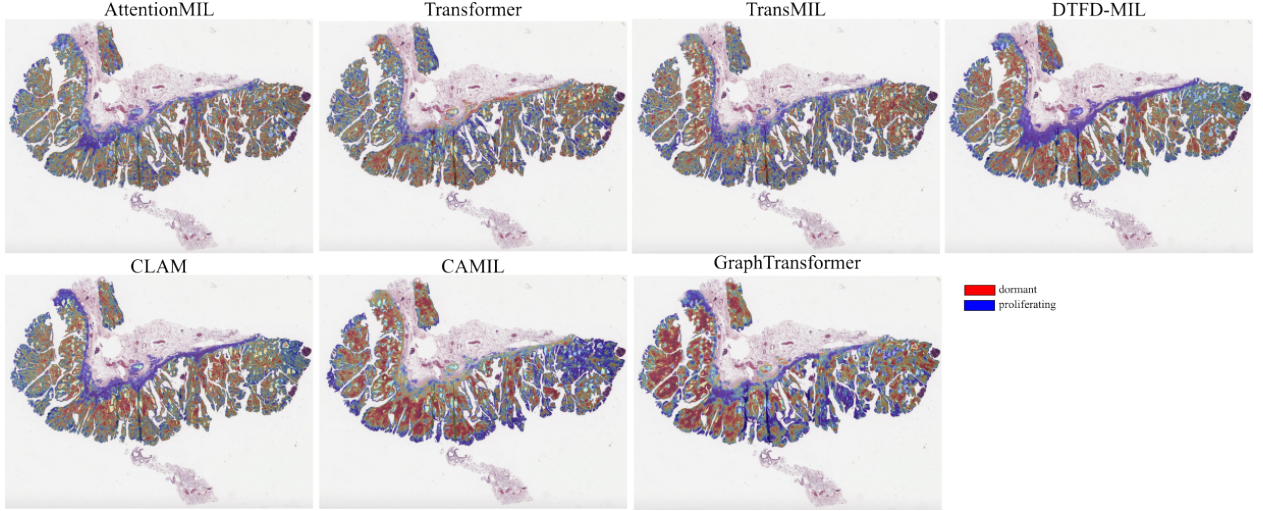


Figure 4: Side-by-side comparison of heatmaps generated by benchmarked algorithms using the UNI feature encoder. Each heatmap is obtained by mapping the average attention scores from an ensemble of the best models per CV fold. All heatmaps explain a TP prediction except for AttentionMIL and GraphTransformer which erroneously make a slide-level prediction of 0. Red indicates high attention scores corresponding to regions with high likelihood of cells in G0-arrest, while blue regions correspond to proliferating cells. Gaussian blur has been applied to avoid a strict demarcation of the patches.

#### 4.4 Limitations and future work

**G0-arrest and tumor heterogeneity.** Our main interest revolves around guiding therapy to be effective against CRC tissue with populations of G0-arrest tumor cells. However, we note that our slide-level labels are computed from bulk-RNA, thus there is a mix of signals which is not unique to tumor cells, but also from a mixture of fibroblasts, immune and endothelial cells in the TME. Future work can exploit ST at a single-cell resolution to demarcate tumor and somatic cells in G0-arrest. Moreover, this can help us evaluate the accuracy of the generated heatmaps, enabling us to answer questions such as whether the use of foundation feature encoders (and with which algorithms), or whether regression-based MIL [El Nahhas et al., 2024], can highlight more biologically-relevant important regions compared to baselines.

**Out-of-distribution evaluation.** We validate our models through 5-fold cross-validation coupled with a TCGA in-domain test-split. Future work can explore the generalization capability of each algorithm through test-splits stratified by different clinical sites [El Nahhas et al., 2024] or datasets belonging to patient cohorts different to TCGA, such as those sourced from the Yorkshire Cancer Research Bowel Cancer Improvement Programme (YCR-BCIP) [Wagner et al., 2023], to evaluate out-of-distribution generalization.

**Graph theory.** Similar to [Parreno-Centeno et al., 2022], we can also resort to graph theory to analyze the cell-cell interactions over a CRC tissue. This method consists of employing nuclei segmentation tools like CellVIT [Horst et al., 2024] or CPP-Net [Chen et al., 2023] over the CRC WSI to build a cell-cell interaction graph. We can then query this graph through knowledge bases like Neo4J to unravel tumour-immune cell dependencies that could be exploited therapeutically. Thus, this would add an additional layer of interpretability analysis to our pipeline, which would prove beneficial for guiding therapy.

**Pan-cancer modelling** Another direction of research worth exploring is predicting the G0-arrest state across cancer tissues [Arslan et al., 2024]. We hypothesize that in this cross-tissue setting, the benefits of employing foundation feature encoders like UNI would be more pronounced compared to our current setting where we only work with CRC tissue. This would greatly increase the size and heterogeneity of our dataset which allows us to perform more thorough evaluation, but it also introduces new challenges since the G0-arrest signature varies by tissue.

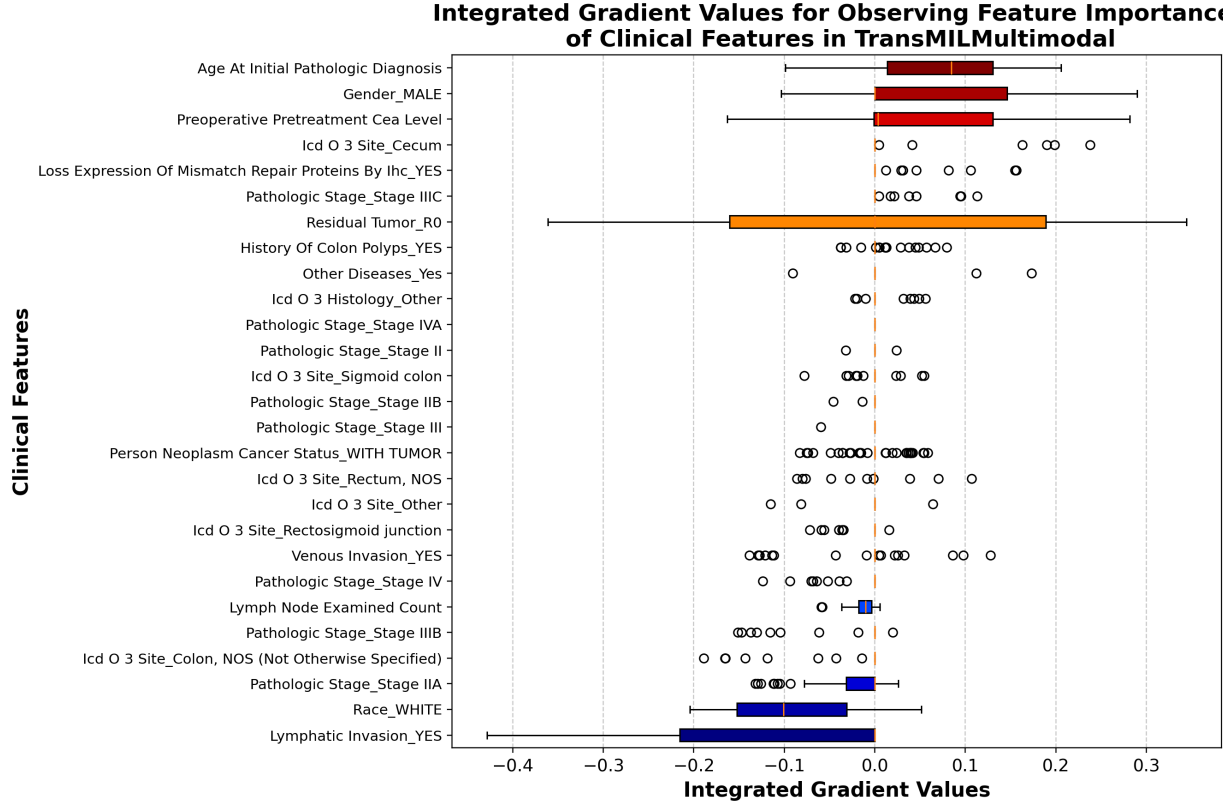


Figure 5: Descendently ranked IG values per clinical feature obtained by averaging the IG values obtained with an ensemble TransMILMultimodal predicting over the test set. We use the same color code as before, except that with IG values, the theoretical range extends to  $[-\infty, +\infty]$ , where positive IG values refer to features contributing to a positive prediction, and vice-versa. IG values of 0 indicate the corresponding features provide no significant information to make a prediction compared to a null baseline.

## 5 Conclusion

We presented PathoInsightMIL as a generalizable framework which enabled us to use deep learning to gauge the G0-arrest population solely from H&E CRC tissue. It encompassed preprocessing WSIs using foundation feature encoders, benchmarking SoTA MIL algorithms and experimenting with ablations, coupled with interpretability analysis which elucidates a model’s internal mechanisms for making a decision. We observe that ensembling, using foundation feature encoders and resorting to regression generally helps with improved test performance. The fusion of clinical features slightly hampered test classification performance, but enabled a thorough discussion of clinical features in the context of studying G0-arrest and relapse. Generated heatmaps provide interpretable results regarding the spatial composition of G0-arrest cells, and graph-based constraints drive them to be more biologically plausible.

Finally, we open source PathoInsightMIL, written in HistoMIL at <https://github.com/awxlong/HistoMIL>, as we are intrigued by how it can be used to understanding the evolution of the tumor landscape and advance cancer research.

## 6 Acknowledgments

We thank Mediha Zukic for sharing her feature selection algorithm used for choosing the clinical features during multimodal fusion. We also extend our gratitude to Dr. Petru Manescu for providing feedback on an earlier draft of our work.

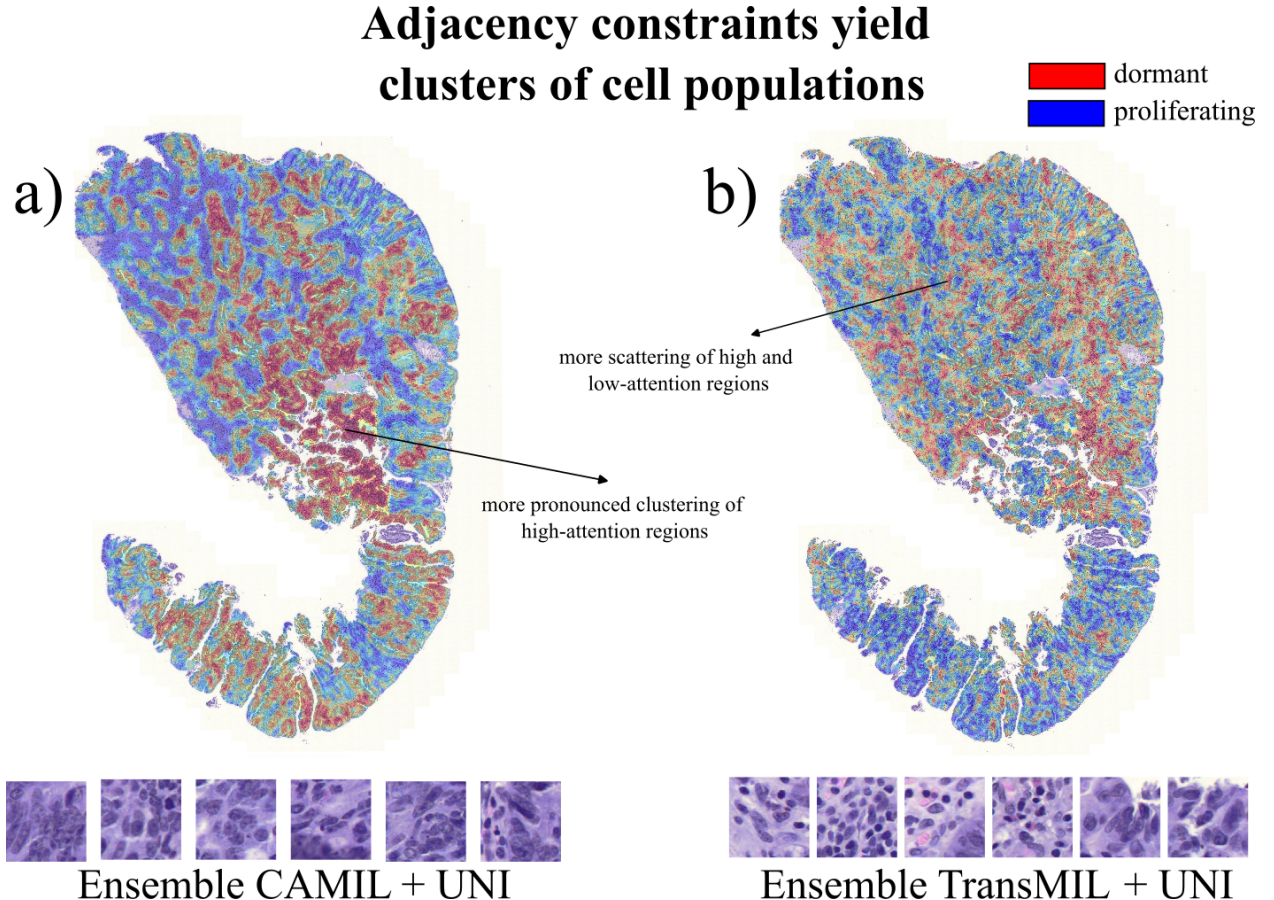


Figure 6: Adjacency constraints introduced via the graph representation of a WSI helps the model visualize more pronounced clusters of cell populations. While this comes at the expense of some performance loss, the spatially-constrained heatmaps produced by a) CAMIL and GraphTransformer align more with biological expectations regarding both the proliferating and quiescent cells to cluster with each other. This is in contrast to b) TransMIL and other algorithms which tend to produce heatmaps with more scattered cell populations. At the bottom of each heatmap we show a sample of 6 patches with the highest attention scores contributing to the TP prediction.

## References

- [Alboaneen et al., 2023] Alboaneen, D., Alqarni, R., Alqahtani, S., Alrashidi, M., Alhuda, R., Alyahyan, E., and Alshammari, T. (2023). Predicting colorectal cancer using machine and deep learning algorithms: Challenges and opportunities. *Big Data and Cognitive Computing*, 7:74.
- [Arslan et al., 2024] Arslan, S., Schmidt, J., Bass, C., Mehrotra, D., Gerald, A., Singhal, S., Hense, J., Li, X., Pandu, R.-L., Maiques, O., Nikolas Kather, J., and Pandya, P. (2024). A systematic pan-cancer study on deep learning-based prediction of multi-omic biomarkers from routine pathology images. *Communications Medicine*, 4.
- [Attaran and Bissell, 2021] Attaran, S. and Bissell, M. J. (2021). The role of tumor microenvironment and exosomes in dormancy and relapse. *Seminars in Cancer Biology*.
- [Azizi et al., 2023] Azizi, S., Culp, L., Freyberg, J., Mustafa, B., Baur, S., Kornblith, S., Chen, T., Tomasev, N., Mitrovic, J., Strachan, P., Mahdavi, S. S., Wulczyn, E., Babenko, B., Walker, M., Loh, A., Chen, P.-H. C., Liu, Y., Bavishi, P., McKinney, S. M., Winkens, J., Roy, A. G., Beaver, Z., Ryan, F., Krogue, J., Etemadi, M., Telang, U., Liu, Y., Peng, L., Corrado, G. S., Webster, D. R., Fleet, D., Hinton, G., Housby, N., Karthikesalingam, A., Norouzi, M., and Natarajan, V. (2023). Robust and data-efficient generalization of self-supervised machine learning for diagnostic imaging. *Nature Biomedical Engineering*, 7:756–779.
- [Baraibar et al., 2023] Baraibar, I., Ros, J., Saoudi, N., Salva, F., García, A., Castells, M. R., Tabernero, J., and Elez, E. (2023). Sex and gender perspectives in colorectal cancer. *ESMO Open*, 8:101204.

- [Chen et al., 2022a] Chen, L., Yang, F., Chen, S., and Tai, J. (2022a). Mechanisms on chemotherapy resistance of colorectal cancer stem cells and research progress of reverse transformation: A mini-review. *Frontiers in Medicine*, 9.
- [Chen et al., 2024] Chen, R. J., Ding, T., Lu, M. Y., Williamson, D. F. K., Jaume, G., Song, A. H., Chen, B., Zhang, A., Shao, D., Shaban, M., Williams, M., Oldenburg, L., Weishaupt, L. L., Wang, J. J., Vaidya, A., Le, L. P., Gerber, G., Sahai, S., Williams, W., and Mahmood, F. (2024). Towards a general-purpose foundation model for computational pathology. *Nature Medicine*, pages 1–13.
- [Chen et al., 2020] Chen, R. J., Lu, M. Y., Wang, J., Williamson, D. F. K., Rodig, S. J., Lindeman, N. I., and Mahmood, F. (2020). Pathomic fusion: An integrated framework for fusing histopathology and genomic features for cancer diagnosis and prognosis. *IEEE Transactions on Medical Imaging*, pages 1–1.
- [Chen et al., 2022b] Chen, R. J., Lu, M. Y., Williamson, D. F., Chen, T. Y., Lipkova, J., Noor, Z., Shaban, M., Shady, M., Williams, M., Joo, B., and Mahmood, F. (2022b). Pan-cancer integrative histology-genomic analysis via multimodal deep learning. *Cancer Cell*, 40:865–878.e6.
- [Chen et al., 2023] Chen, S., Ding, C., Liu, M., and Tao, D. (2023). Cpp-net: Context-aware polygon proposal network for nucleus segmentation. *IEEE Transactions on Image Processing*, 32:980–994.
- [Cho et al., 2021] Cho, M. Y., Siegel, D. A., Demb, J., Richardson, L. C., and Gupta, S. (2021). Increasing colorectal cancer incidence before and after age 50: Implications for screening initiation and promotion of "on-time" screening. *Digestive Diseases and Sciences*, 67:4086–4091.
- [Cooper, 2000] Cooper, G. M. (2000). The eukaryotic cell cycle.
- [Couture, 2022] Couture, H. D. (2022). Deep learning-based prediction of molecular tumor biomarkers from h&e: A practical review. *Journal of Personalized Medicine*, 12:2022.
- [El Nahhas et al., 2024] El Nahhas, O., Chiara, L., Carrero, Z. I., Treeck, M. v., Kolbinger, F. R., Hewitt, K. J., Muti, H. S., Graziani, M., Zeng, Q., Calderaro, J., Ortiz-Brüchle, N., Yuan, T., Hoffmeister, M., Brenner, H., Brobeil, A., Reis-Filho, J. S., and Nikolas Kather, J. (2024). Regression-based deep-learning predicts molecular biomarkers from pathology slides. *Nature Communications*, 15.
- [Feng et al., 2024] Feng, X., Shu, W., Li, M., Li, J., Xu, J., and He, M. (2024). Pathogenomics for accurate diagnosis, treatment, prognosis of oncology: a cutting edge overview. *Journal of translational medicine*, 22.
- [Fourkioti et al., 2024] Fourkioti, O., De Vries, M., and Bakal, C. (2024). Camil: Context-aware multiple instance learning for cancer detection and subtyping in whole slide images. *The Twelfth International Conference on Learning Representations*.
- [Gadermayr and Tschuchnig, 2024] Gadermayr, M. and Tschuchnig, M. (2024). Multiple instance learning for digital pathology: A review of the state-of-the-art, limitations & future potential. *Computerized Medical Imaging and Graphics*, pages 102337–102337.
- [Geddes et al., 2022] Geddes, A. E., Ray, A. L., Nofchissey, R. A., Esmaeili, A., Saunders, A., Bender, D. E., Khan, M., Sheeja, A., Ahrendsen, J. T., Li, M., Fung, K.-M., Jayaraman, M., Yang, J., Booth, K. K., Dunn, G. D., Carter, S. N., and Morris, K. T. (2022). An analysis of sexual dimorphism in the tumor microenvironment of colorectal cancer. *Frontiers in Oncology*, 12.
- [Hezi et al., 2024] Hezi, H., Gelber, M., Balabanov, A., Yosef E, M., and Freiman, M. (2024). Cimil-crc: a clinically-informed multiple instance learning framework for patient-level colorectal cancer molecular subtypes classification from h&e stained images. *arXiv (Cornell University)*.
- [Horst et al., 2024] Horst, F., Rempe, M., Heine, L., Seibold, C., Keyl, J., Baldini, G., Ugurel, S., Siveke, J., Grünwald, B., Egger, J., and Kleesiek, J. (2024). Cellvit: Vision transformers for precise cell segmentation and classification. *Medical image analysis*, 94:103143–103143.
- [Ilse et al., 2018] Ilse, M., Tomczak, J., and Welling, M. (2018). Attention-based deep multiple instance learning. *proceedings.mlr.press*, pages 2127–2136.
- [Lai et al., 2023] Lai, Y.-H., Chang, Y.-T., Chang, Y.-J., Tsai, J.-T., Li, M.-H., and Lin, J.-C. (2023). Predictive value of the interaction between cea and hemoglobin in neoadjuvant ccrt outcomes in rectal cancer patients. *Journal of Clinical Medicine*, 12:7690–7690.
- [Lawrence et al., 2023] Lawrence, R., Watters, M., Davies, C. R., Pantel, K., and Lu, Y.-J. (2023). Circulating tumour cells for early detection of clinically relevant cancer. *Nature Reviews Clinical Oncology*, 20:487–500.
- [Lee, 2023] Lee, M. (2023). Recent advancements in deep learning using whole slide imaging for cancer prognosis. *Bioengineering*, 10:897–897.

- [Levy-Jurgenson et al., 2020] Levy-Jurgenson, A., Tekpli, X., Kristensen, V. N., and Yakhini, Z. (2020). Spatial transcriptomics inferred from pathology whole-slide images links tumor heterogeneity to survival in breast and lung cancer. *Scientific Reports*, 10.
- [Lindell et al., 2023] Lindell, E., Zhong, L., and Zhang, X. (2023). Quiescent cancer cells—a potential therapeutic target to overcome tumor resistance and relapse. *International Journal of Molecular Sciences*, 24:3762–3762.
- [Lu et al., 2021] Lu, M. Y., Williamson, D. F. K., Chen, T. Y., Chen, R. J., Barbieri, M., and Mahmood, F. (2021). Data-efficient and weakly supervised computational pathology on whole-slide images. *Nature Biomedical Engineering*, 5:555–570.
- [Martino et al., 2024] Martino, F., Ilardi, G., Varricchio, S., Russo, D., Maria, R., Staibano, S., and Merolla, F. (2024). A deep learning model to predict ki-67 positivity in oral squamous cell carcinoma. *Journal of Pathology Informatics*, 15:100354–100354.
- [Messenger et al., 2012] Messenger, D. E., Driman, D. K., and Kirsch, R. (2012). Developments in the assessment of venous invasion in colorectal cancer: implications for future practice and patient outcome. *Human Pathology*, 43:965–973.
- [Mitra et al., 2018] Mitra, M., Ho, L. D., and Coller, H. A. (2018). An in vitro model of cellular quiescence in primary human dermal fibroblasts. *Methods in molecular biology (Clifton, N.J.)*, 1686:27–47.
- [Nadorvari et al., 2024] Nadorvari, M. L., Lotz, G., Kulka, J., Kiss, A., and Timar, J. (2024). Microsatellite instability and mismatch repair protein deficiency: equal predictive markers? *Pathology & Oncology Research*, 30.
- [Oki et al., 2014] Oki, T., Nishimura, K., Kitaura, J., Togami, K., Maehara, A., Izawa, K., Sakaue-Sawano, A., Niida, A., Miyano, S., Aburatani, H., Kiyonari, H., Miyawaki, A., and Kitamura, T. (2014). A novel cell-cycle-indicator, mvenus-p27k-, identifies quiescent cells and visualizes g0-g1 transition. *Scientific Reports*, 4.
- [Pack et al., 2019] Pack, L. R., Daigh, L. H., and Meyer, T. (2019). Putting the brakes on the cell cycle: mechanisms of cellular growth arrest. *Current Opinion in Cell Biology*, 60:106–113.
- [Park and Nam, 2020] Park, S.-Y. and Nam, J.-S. (2020). The force awakens: metastatic dormant cancer cells. *Experimental & Molecular Medicine*, 52:569–581.
- [Parreno-Centeno et al., 2022] Parreno-Centeno, M., Malagoli Tagliazucchi, G., Withnell, E., Pan, S., and Secrier, M. (2022). A deep learning and graph-based approach to characterise the immunological landscape and spatial architecture of colon cancer tissue. *bioRxiv (Cold Spring Harbor Laboratory)*.
- [Qaderi et al., 2021] Qaderi, S. M., Galjart, B., Verhoef, C., Slooter, G. D., Koopman, M., Verhoeven, R. H. A., de Wilt, J. H. W., and van Erning, F. N. (2021). Disease recurrence after colorectal cancer surgery in the modern era: a population-based study. *International Journal of Colorectal Disease*, 36:2399–2410.
- [Safari et al., 2023] Safari, M., Mahmoudi, L., Baker, E. K., Roshanaei, G., Fallah, R., Shahnavaz, A., and Asghari-Jafarabadi, M. (2023). Recurrence and postoperative death in patients with colorectal cancer: A new perspective via semi-competing risk framework. *PubMed Central*, 34:736–746.
- [Sallinger et al., 2023] Sallinger, K., Gruber, M., Müller, C.-T., Bonstingl, L., Pritz, E., Pankratz, K., Gerger, A., Smolle, M. A., Aigelsreiter, A., Surova, O., Svedlund, J., Nilsson, M., Kroneis, T., and El-Heliebi, A. (2023). Spatial tumour gene signature discriminates neoplastic from non-neoplastic compartments in colon cancer: unravelling predictive biomarkers for relapse. *Journal of translational medicine*, 21.
- [Schirris et al., 2022] Schirris, Y., Gavves, E., Nederlof, I., Horlings, H. M., and Teuwen, J. (2022). Deepsmile: Contrastive self-supervised pre-training benefits msi and hrh classification directly from h&e whole-slide images in colorectal and breast cancer. *Medical Image Analysis*, 79:102464.
- [Shao et al., 2021] Shao, Z., Bian, H., Chen, Y., Wang, Y., Zhang, J., Ji, X., and zhang, y. (2021). Transmil: Transformer based correlated multiple instance learning for whole slide image classification. *Advances in Neural Information Processing Systems*, 34:2136–2147.
- [Shi et al., 2024] Shi, Z., Zhang, J., Kong, J., and Wang, F. (2024). Integrative graph-transformer framework for histopathology whole slide image representation and classification. *Lecture notes in computer science*, pages 341–350.
- [Song et al., 2023] Song, A. H., Jaume, G., Williamson, D., Lu, M., Vaidya, A., Miller, T. R., and Mahmood, F. (2023). Artificial intelligence for digital and computational pathology. *Nature Reviews Bioengineering*.
- [Sundararajan et al., 2017] Sundararajan, M., Taly, A., and Yan, Q. (2017). Axiomatic attribution for deep networks. *Proceedings of the 34th International Conference on Machine Learning - Volume 70*, 70:3319–3328.

- [Tan et al., 2023] Tan, L., Li, H., Yu, J., Zhou, H., Wang, Z., Niu, Z., Li, J., and Li, Z. (2023). Colorectal cancer lymph node metastasis prediction with weakly supervised transformer-based multi-instance learning. *Medical & Biological Engineering & Computing*, 61:1565–1580.
- [Thoma et al., 2021] Thoma, O.-M., Neurath, M. F., and Waldner, M. J. (2021). T cell aging in patients with colorectal cancer - what do we know so far? *Cancers*, 13:6227.
- [Tran et al., 2021] Tran, K. A., Kondrashova, O., Bradley, A., Williams, E. D., Pearson, J. V., and Waddell, N. (2021). Deep learning in cancer diagnosis, prognosis and treatment selection. *Genome Medicine*, 13.
- [Truskowski et al., 2023] Truskowski, K., Amend, S. R., and Pienta, K. J. (2023). Dormant cancer cells: programmed quiescence, senescence, or both? *Cancer and Metastasis Reviews*, 42:37–47.
- [Volinsky-Fremond et al., 2024] Volinsky-Fremond, S., Horeweg, N., Andani, S., Barkey Wolf, J., Lafarge, M. W., de Kroon, C. D., Ortoft, G., Hogdall, E., Dijkstra, J., Jobsen, J. J., Lutgens, L. C. H. W., Powell, M. E., Mileshkin, L. R., Mackay, H., Leary, A., Katsaros, D., Nijman, H. W., de Boer, S. M., Nout, R. A., de Bruyn, M., Church, D., Smit, V. T. H. B. M., Creutzberg, C. L., Koelzer, V. H., and Bosse, T. (2024). Prediction of recurrence risk in endometrial cancer with multimodal deep learning. *Nature Medicine*, pages 1–12.
- [Vorontsov et al., 2023] Vorontsov, E., Bozkurt, A., Casson, A., Shaikovski, G., Zelechowski, M., Liu, S., Mathieu, P., van Eck, A., Lee, D., Viret, J., Robert, E., Wang, Y. K., Kun, J., Le, M., Bernhard, J., Godrich, R., Oakley, G. J., Millar, E. K., Hanna, M. G., Retámero, J. A., Moye, W. A., Yousfi, R., Kanan, C., Klimstra, D. S., Rothrock, B., and Fuchs, T. J. (2023). Virchow: A million-slide digital pathology foundation model. *arXiv (Cornell University)*.
- [Wagner et al., 2023] Wagner, S. J., Reisenbüchler, D., West, N. P., Moritz Niehues, J., Zhu, J., Foersch, S., Patrick Veldhuizen, G., Quirke, P., Grabsch, H., , v., Hutchins, G., Richman, S. D., Yuan, T., Langer, R., Jenniskens, J. C. A., Offermans, K., Mueller, W., Gray, R., Gruber, S. B., Greenson, J. K., Rennert, G., Bonner, J. D., Schmolze, D., Jonnagaddala, J., Hawkins, N. J., Ward, R. L., Morton, D., Seymour, M., Magill, L., Nowak, M., Hay, J., Koelzer, V. H., Church, D. N., Matek, C., Geppert, C., Peng, C., Zhi, C., Ouyang, X., James, J., Loughrey, M. B., Salto-Tellez, M., Brenner, H., Hoffmeister, M., Truhn, D., Schnabel, J. A., Boxberg, M., Peng, T., Nikolas Kather, J., Church, D. N., Domingo, E., Edwards, J., Glimelius, B., Gögenür, I., Harkin, A., Hay, J., Iveson, T., Jaeger, E., Kelly, C., Kerr, R., Maka, N., Morgan, H., Oien, K. A., Orange, C., Palles, C., Roxburgh, C. S., Sansom, O. J., Saunders, M., and Tomlinson, I. (2023). Transformer-based biomarker prediction from colorectal cancer histology: A large-scale multicentric study. *Cancer Cell*, 41:1650–1661.e4.
- [Wiecek et al., 2023] Wiecek, A. J., Cutty, S. J., Kornai, D., Parreno-Centeno, M., Gourmet, L. E., Malagoli Tagliazucchi, G., Jacobson, D. H., Zhang, P., Xiong, L., Bond, G. L., Barr, A. R., and Secrier, M. (2023). Genomic hallmarks and therapeutic implications of g0 cell cycle arrest in cancer. *Genome Biology*, 24.
- [Xiao et al., 2024] Xiao, H., Weng, Z., Sun, K., Shen, J., Lin, J., Chen, S., Li, B., Shi, Y., Kuang, M., Song, X., Weng, W., and Peng, S. (2024). Predicting 5-year recurrence risk in colorectal cancer: development and validation of a histology-based deep learning approach. *British Journal of Cancer*, 130:951–960.
- [Xu et al., 2024] Xu, H., Usuyama, N., Bagga, J., Zhang, S., Rao, R., Naumann, T., Wong, C., Gero, Z., González, J., Gu, Y., Xu, Y., Wei, M., Wang, W., Ma, S., Wei, F., Yang, J., Li, C., Gao, J., Rosemon, J., Bower, T., Lee, S., Weerasinghe, R., Wright, B. J., Robicsek, A., Piening, B., Bifulco, C., Wang, S., and Poon, H. (2024). A whole-slide foundation model for digital pathology from real-world data. *Nature*, pages 1–8.
- [Yacob et al., 2023] Yacob, F., Siarov, J., Williamsson, K., Suvilehto, J. T., Sjöblom, L., Kjellberg, M., and Neittaanmäki, N. (2023). Weakly supervised detection and classification of basal cell carcinoma using graph-transformer on whole slide images. *Scientific Reports*, 13.
- [Zhang et al., 2022] Zhang, H., Meng, Y., Zhao, Y., Qiao, Y., Yang, X., Coupland, S. E., and Zheng, Y. (2022). Dtfdmil: Double-tier feature distillation multiple instance learning for histopathology whole slide image classification. *2022 IEEE/CVF Conference on Computer Vision and Pattern Recognition (CVPR)*.
- [Zheng et al., 2022] Zheng, Y., Gindra, R., Green, E. J., Burks, E., Betke, M., Beane, J., and Kolachalam, V. B. (2022). A graph-transformer for whole slide image classification. *IEEE Transactions on Medical Imaging*, 41:3003–3015.
- [Zukic, 2024] Zukic, M. (2024). Predict schizophrenia using brain anatomy. *Applied AI (COMP0189) coursework*.

## A Multiple instance learning.

The gigapixel resolution and thus complexity of WSIs present unique computational challenges for the design of a DL pipeline to analyze them. The typical paradigm of pre-processing WSIs consists of tissue segmentation, followed a patch-wise cropping step which divides the gigapixel tissue into thousands of square patches with smaller dimensions, e.g.,  $224 \times 224$  pixels. They are then passed to a feature encoder to obtain a feature representation  $\mathcal{W} \in \mathbb{R}^{N \times D}$  of the

WSI, where  $N$  is the number of patches and  $D$  is the dimension of the vector output by the feature encoder. Patch-wise embeddings are aggregated through pooling methods to obtain a global prediction [Tan et al., 2023].

Only slide-level labels are available due to the intense annotation burden associated with WSIs [Tan et al., 2023, Gadermayr and Tschuchnig, 2024]. A WSI is represented as a 'bag'  $B^n$ , which is a collection of patches, or 'instances',  $\{x_1^n, x_2^n, \dots, x_d^n\}$ , where each  $B^n$  is given single label  $y^n$  as follows:

$$y^n = \begin{cases} s & \text{if } \exists j \text{ such that } x_j^n = 1 \\ 0 & \text{if } \forall j, x_j^n = 0 \end{cases} \quad (2)$$

, where  $s \in \{0, 1\}$  in a binary classification task, e.g., predicting the presence/absence of G0-arrest cells, or  $s \in \mathbb{R}$  if we are predicting a score for the state of G0-arrest. This is, if in certain regions of the tissue G0-arrest cells are identified, then the entire WSI receives a positive label.

Due to this problem setup, we resort to a ***multiple-instance learning*** (MIL) framework, a form of weakly-supervised learning. The goal is to learn to classify slides, as well as the key patches that 'trigger' the slide's label. We train such classifier  $f$  by optimizing the negative log likelihood of its parameters  $\theta$ :

$$-\mathcal{LL}(\mathcal{D}|\theta) = \sum_{i=1}^N \ell(y^i, \hat{y}^i) \quad (3)$$

, where  $\hat{y}^i = \max_j f(x_j^n)$  can be the max pooling over the  $N$  instance embeddings in a bag to determine the bag's label,  $\hat{y}^i = \sum_{j=1}^N f(x_{ij})$  a sum pooling of all embeddings within the bag, or  $\hat{y}^i = \frac{1}{N} \sum_{j=1}^N f(x_j)$  can be mean pooling which computes the average of all instance embeddings in the bag (implicitly treating all of them equally), which is not necessarily the case for WSIs where tumour tissue is more relevant for the task. For each pooling method, the instance embeddings can have attention scores,  $\alpha$ , which act as weights representing their relative contribution to the final prediction, e.g.,  $\hat{y}^i = \frac{1}{N} \sum_{j=1}^N \alpha_j f(x_j)$ . These attention scores are inherently interpretable as they can be traced back to the original WSI input space, highlighting regions of interest.  $\ell$  is a loss function depending on the output and label modality, which could be the mean squared error in the continuous case, or binary-cross entropy in the discrete case. The choice of architectural backend of  $f$ , and the modality of the output (multimodal vs. regression vs. classification) are highly customizable depending on the task specifications and available computational resources.

## B 5-fold cross-validation results

Our cross-validation (CV) results for each feature encoder and MIL algorithm are shown at Figure 7 for the AUROC metric and at Figure 8 for the F1. Uncertainty regions correspond to the standard deviations of the metric averaged across folds, and these are spread across epochs. We notice much overlap amongst the regions of different feature encoders, which indicates that during cross-validation, the use of foundation feature encoders didn't show much performance improvement.

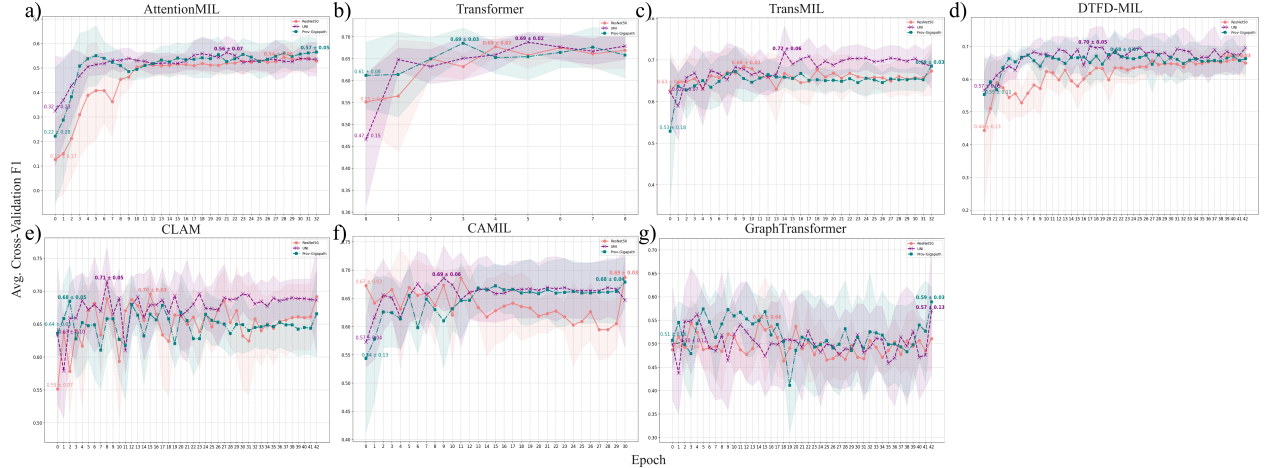


Figure 8: Average F1 across folds per epoch shown per classifier. We label two "milestones" in the same manner as in Figure 7, where we observe that the highest mean cross-validation F1 is not necessarily achieved at the end of training.

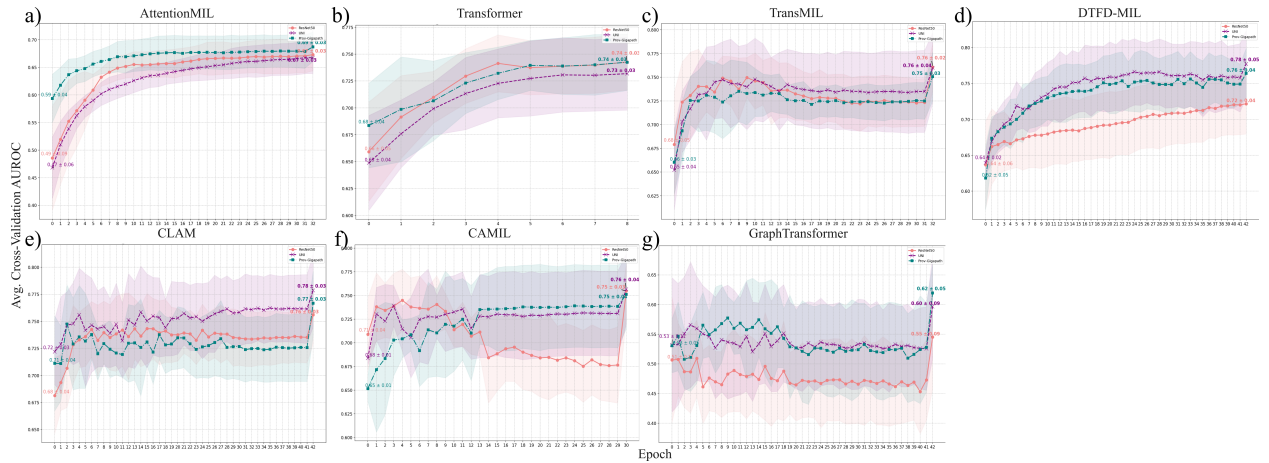


Figure 7: Average AUROC across folds per epoch shown per classifier. We label two "milestones", which is the average performance at the beginning of training, and in bold we show the highest mean cross-validation AUROC achieved at the end of training to illustrate the improvement brought by learning. There is much overlap in CV AUROC's uncertainty regions, with occasional noticeable demarcation such as in d) where the ResNet50 encoder consistently yields lower performance across epochs than its foundation model alternatives.

Our CV results help guide how we further explore multimodal fusion and regression by pruning the space of all possible experiments to run, i.e., we avoid exhaustive ablation exploring multimodal fusion with all MIL algorithms and feature encoders. From the plots, we generally observe that classifier consisting of the Prog-Gigapath and UNI feature encoders have slightly higher mean performance than ResNet50. In addition, TransMIL is the one which achieves amongst the highest CV AUROC ( $\approx 0.75$ ) and highest mean CV F1-score ( $0.72 \pm 0.06$ ) (albeit it's closely followed by CLAM and DTFD-MIL). Because of this, we explore multimodal fusion of clinical features and outputting regression scores only with TransMIL with the UNI feature encoder.

We only show the mean CV F1 across folds in Figure 9 because PCC is not available for the base TransMIL and TransMILMultimodal, while AUROC is not available for TransMILRegression. In this regard, F1 provides a common score to compare ablations of TransMIL.

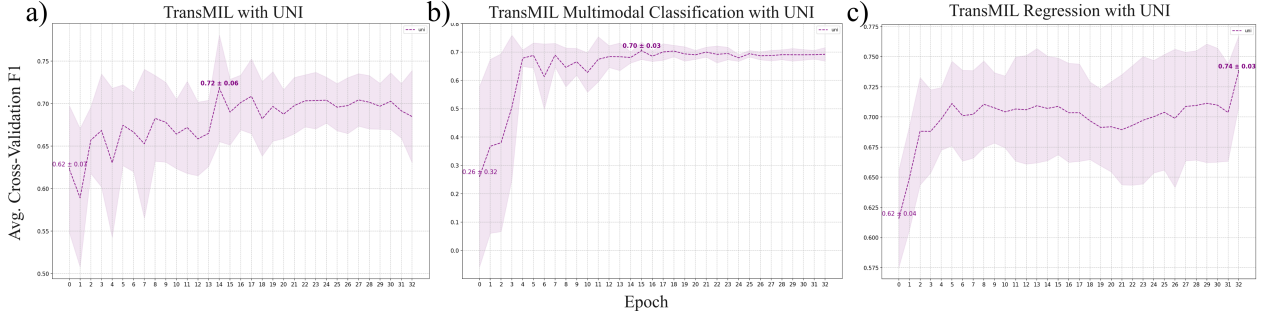


Figure 9: Average F1 across folds per epoch shown for ablations of TransMIL with UNI: TransMILMultimodal and TransMILRegression. We label two "milestones" in the same manner as in Figure 7. a) is the same lineplot as Figure 8c's UNI encoder. b) Interestingly, the average scores across folds is more stable, suggesting that multimodal fusion stabilizes training across folds.

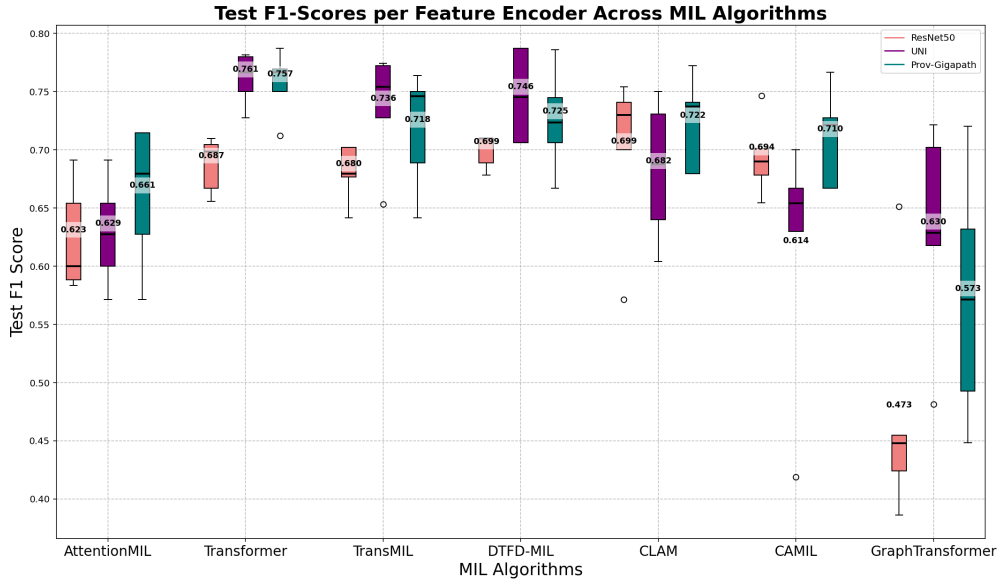


Figure 10: Boxplot of test F1 scores obtained from the 5 independent optimal models per fold, per feature encoder, evaluated over the test set. The often higher test scores (i.e. higher purple and teal bars) achieved by the UNI and Prov-Gigapath feature encoders suggests better generalization capabilities brought by foundation feature encoders in comparison to the standard ImageNet-pretrained ResNet50.

## C Test results

## D Clinical feature selection and preprocessing

Clinical features are accessible for our 570 patients at TCGA. However, prior to processing, a lot of features are ignored due to any of the following reasons:

- biological irrelevance for predicting cell senescence: corresponds to features which are uninformative to predict the G0-arrest label. This includes: name of the clinic in which the tissue was sourced, height, whether patient consent was verified, and number of first degree relatives with cancer diagnosis.
- constant-valued variables: corresponds to features mostly filled with a constant value such as primary lymph node presentation assessment where 98% of the values were YES.
- semantically-same variables: corresponds to features which arguably refer to the same measurements, and thus were dropped to avoid multicollinearity. For example, if we include count of lymph nodes as part of our multimodal model, we drop count of lymph nodes by H&E and by IHC. Similarly, we drop ICD-O-10 for ICD-O-3, and exclude anatomic neoplasm subdivision because of ICD-O-3 site.

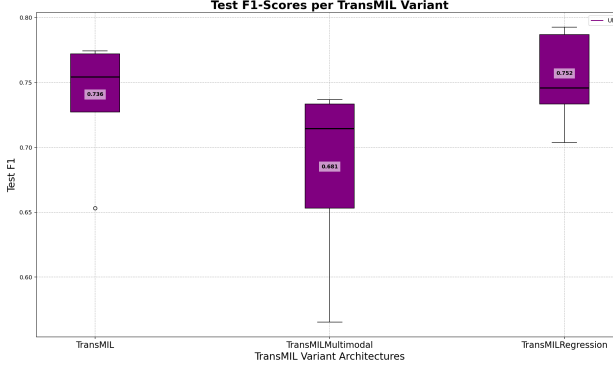


Figure 11: Boxplot of test F1 scores obtained from the 5 independent optimal TransMIL ablation models per fold, trained using the UNI encoder, evaluated over the test set.

---

**Algorithm 1** Feature selection based on shadow features adapted from [Zukic, 2024].

---

```

1: Input:  $X_{train}$ ,  $y_{train}$ , classifier,  $n_{iter} = 100$ , threshold= 42
2: Output: indexes of features selected from  $X_{train}$ 
3:  $n, d = X_{train}.shape$ 
4: scores = zeros(d)                                      $\triangleright$  zero vector of shape d
5:  $X_{train} = \text{join}(X_{train}, \text{rand\_col})$            $\triangleright$  join a random column of features to  $X_{train}$ 
6: scale( $X_{train}$ )                                      $\triangleright$  min_max, normalize, robust_scaling, among others
7: for  $i = 0 : n_{iter}$  do
8:   classifier(random_state = i).fit( $X_{train}, y_{train}$ )
9:   feature_importances = get_feature_importances(classifier)
10:  rand_col_imp = feature_importances[-1]                 $\triangleright$  Get the random column feature's importance
11:  scores[argwhere(feature_importances > rand_col_imp)]  $\pm 1$             $\triangleright$  Count the times in which a feature's
      importance exceeds that of the random column feature's importance
12: end for
13: return argwhere(scores > threshold)

```

---

After this, preprocessing occurs as follows:

1. We split the train-validation-test set for the clinical patient dataset, and take care in normalizing the continuous variables avoiding train-validation and train-test leakage. We save the features as tensors per patient for each CV fold and test set which is accessed separately during model training and evaluation.
2. A lot of variables concerning radiation therapy, e.g., drug administered, and its amount administered were dropped since they have a greater than 60% missing rate.
3. Variables like race and histological site have some of their values grouped to address class imbalance. For example, in our TCGA clinical dataset's training split, the variable 'race' consists of 4 values with ratios indicating severe imbalance: White (76%), Black (20%), Asian (3%) and American Indian (1%). We thus group 'Black', 'Asian' and 'American Indian' under 'Non-White' and treat 'race' as a binary variable.
4. One variable per each one-hot encoded categorical variables is dropped to avoid multicollinearity. This is valid due to the mutual exclusivity of the values of the categorical variables. For example, one-hot encoding Pathological Stage with 9 possible values leads to the binary variables Pathological Stage I, Pathological Stage II(A, B), Pathological Stage III(B,C), and Pathological Stage IV(A) being formed. For example, a value of 1 for Pathological Stage IIA and 0 for the rest indicates this patient's CRC tissue is in Pathological Stage IIA. Since we assume cancer tissue cannot be at multiple stages simultaneously, and can only be in either of the described stages, Stage I is dropped to avoid collinearity as it is equivalent all remaining binary variables being set to 0.
5. One-hot encoding yields 30 features. We run a feature selection algorithm [Zukic, 2024] which selects 27 out of these 30 features. Feature selection (Algorithm 1) consists of training a classifier (in our case XGBoost) where a random feature vector is concatenated to the above preprocessed dataset to predict g0-arrest. Feature importances are computed, and for those with importance scores below that of the random feature vector's are recorded in a counter. Such process is repeated for  $n = 100$  times, and we get rid of 3 features 'Pathologic

Stage IIC', 'Pathologic Stage IIIA', and 'Pathologic Stage IVB' which for more than 42 times, their feature importances didn't exceed that of the random feature vector's.

6. This is finally followed by expert consultation with a computational biologist to ensure their relevance for multimodal fusion in our model.

We end up with the following list of clinical features:

- patient's age at the time of pathological diagnosis, which we treat as a normalized continuous variable.
- count of lymph nodes observable in the patient's tissue, which we treat as a normalized continuous variable.
- preoperative CEA level, which is treated as a normalized continuous variable. It refers to CEA in the blood before surgical intervention in CRC patients and serves as a tumor progression marker to guide therapy.
- gender, a binary variable with values 'male' and 'female'.
- race, a binary variable with values 'white' and 'non-white'
- other diagnoses, a binary variable indicating whether the patient has comorbidities
- pathological stage, a categorical variable with values stages II, IIA, IIB, III, IIIB, IIIC, IV, IVA. Stages II, IIA and IIB are also known as early stage cancer, while the remaining ones can be clustered under late stage cancer. Metastasis is one of the main markers differentiating these cancer stages.
- histological site, which is a categorical variable indicating tumor anatomical site following the Third Edition of the International Classification of Diseases for Oncology (ICD-O-3). Values include the 'cecum', 'colon, not otherwise specified (NOS)', 'rectosigmoid junction', 'rectum, NOS', 'sigmoid colon' and 'other'.
- patient's neoplasm cancer status, which is a binary variable indicating whether there's an observable tumor or not in the tissue.
- venous invasion, which is a binary variable referring to the presence of tumor cells within blood vessels outside the colorectal wall.
- lymphatic invasion, which is a binary variable referring to the presence of tumor cells within lymphatic vessel. Both venous and lymphatic invasion are markers of metastasis and recurrence [Messenger et al., 2012].
- history of colon polyps, which is a binary variable indicating whether patient has developed polyps or not. Morphological details about the polyps are not provided.
- residual tumor, which is a binary variable indicating the presence of cancerous tissue after treatment, such as post-surgical resection.
- loss of expression of mismatch repair (MMR) proteins as detected by immunohistochemistry (IHC), which is a binary variable referring to whether there's a complete absence of nuclear staining for MMR proteins indicating inability to correct DNA replication errors. It serves as a biomarker for increased potential for tumorigenesis [Nadorvari et al., 2024].

## E Hyperparameters of the MIL models benchmarked

We proceed in stating relevant hyperparameters of MIL models benchmarked.

## F Interpretability analysis of Ensemble TransMIL with UNI feature encoder

	Epoch	Initial learning rate, and weight decay	Optimizer	Learning rate scheduling policy	Additional hyperparameters
AttentionMIL	32	$2 \times 10^{-5}, 1 \times 10^{-2}$	Adam	fit-one-cycle with a maximum learning rate of $1 \times 10^{-4}$ , and the first 25% of the cycle with increasing learning rate (Wang et al., 2022)	
Transformer	8	$2 \times 10^{-5}, 2 \times 10^{-5}$	AdamW	cosine annealing decaying over training epochs with a minimum learning rate of $1 \times 10^{-6}$	
TransMIL	32	$2 \times 10^{-5}, 1 \times 10^{-2}$	AdamW	same as Transformer	
DTFD-MIL	42	$2 \times 10^{-5}, 1 \times 10^{-4}$	Adam for both tiers	learning rate decay starts at epoch 25 for both tiers by a factor of 0.2	5pseudo-bags
CLAM	42	$2 \times 10^{-4}, 1 \times 10^{-5}$	Adam	same as Transformer	dropout of 0.25 and 8 patches for instance-level clustering
CAMIL	30	$2 \times 10^{-5}, 2 \times 10^{-5}$	Adam	learning rate is reduced by a factor of 0.2 once a plateau in performance is identified	
GraphTransformer	42	$1 \times 10^{-3}, 5 \times 10^{-4}$	Adam	learning rate decay starts at epoch 20 by a factor of 0.1	
TransMILMultimodal				same as TransMIL	27 clinical features
TransMILRegression				same as TransMIL	MSE loss

Table 3: Hyperparameters adopted per MIL algorithm. For each algorithm, we embed the source where the hyperparameters are mentioned. We avoid hyperparameter tuning, and this includes not performing extensive neural architecture search. Unless stated otherwise, all models are trained by minimizing the BCEWithLogits loss. TransMILRegression is trained with the MSELoss.

## Ensemble TransMIL + UNI (AUROC: 0.829 - F1: 0.724)

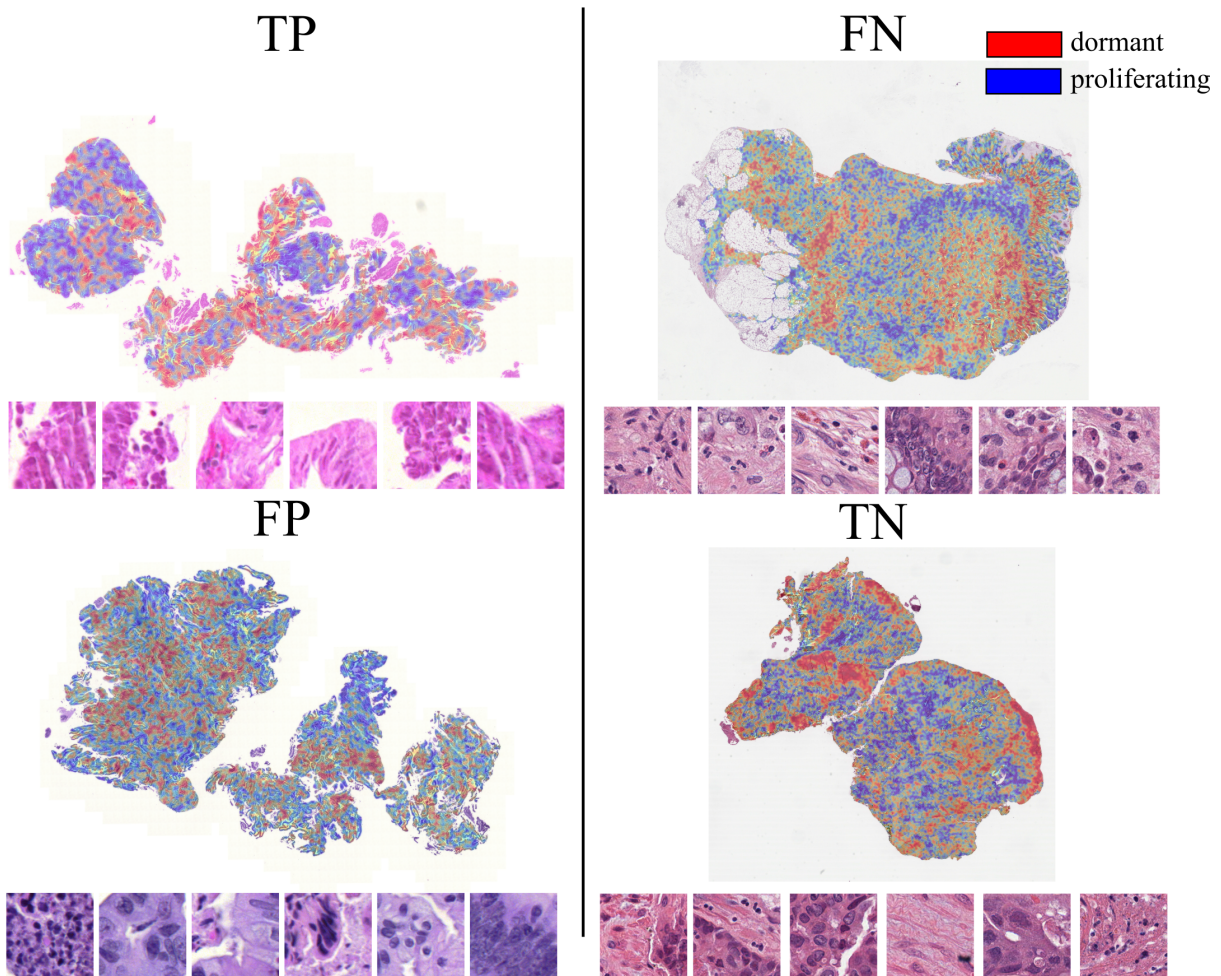


Figure 12: Heatmaps generated by the Ensemble TransMIL with the UNI feature encoder. We provide correct and incorrect classifications, and below each heatmap we append a sample of 6 patches according to their attention scores contributing to the slide-level prediction. For TP and FP, these patches have the highest attention scores explaining a positive prediction. For TN and FN, the patches have the lowest attention scores explaining a negative prediction.

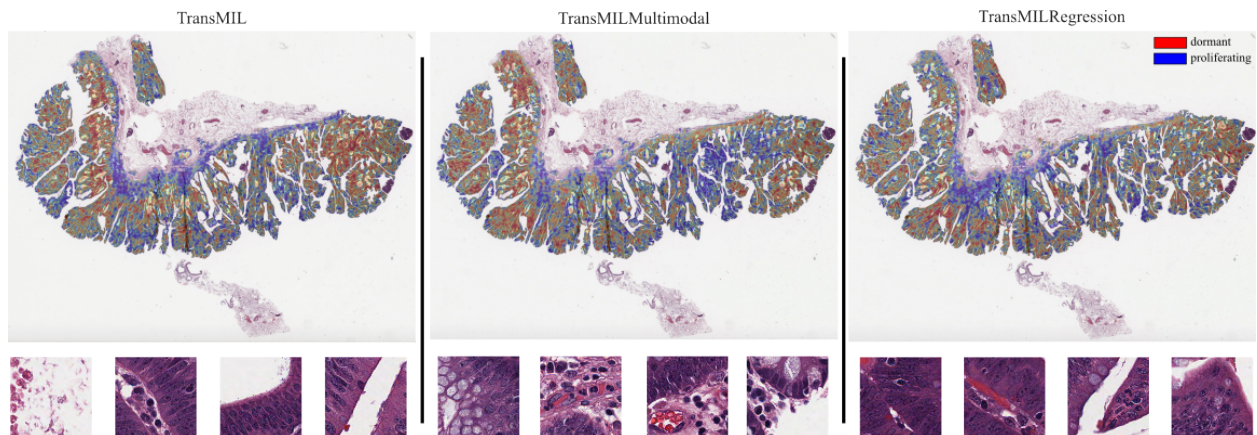


Figure 13: Side-by-side comparison of heatmaps generated by ablations of TransMIL with the UNI feature encoder. Below each heatmap is a sample of 4 patches with the highest attention scores contributing to the prediction of G0-arrest, and are all TP predictions. For TransMIL and TransMILMultimodal, this corresponds to a prediction of 1, while for TransMILRegression, this is a negative score of  $-0.39$  with ground truth  $-2.1$  binarized at  $\leq 0$